Research Article

Environmental Chemistry and Safety
DOI: 10.26599/ECS.2025.9600058
2026, 2, 9600058

Ultrasound-Fabricated $BaZrO_3$ Nanoneedles for Degradation of Hazardous Organic Dyes

Harsha Chavan, Aruna M. Sudapalli, and Purav M. Badani*

Department of Chemistry, University of Mumbai Santa Cruz (E), Mumbai- 400098, Maharashtra, India

Abstract: Ultrasound-assisted cavitation was used to synthesize $BaZrO_3$ nanoneedles. Ultrasonic energy facilitated uniform mixing and anisotropic growth along the c-axis, resulting in a needle-like shape. The synthesized $BaZrO_3$ nanoneedles were characterized using X-ray diffraction (XRD) for phase and crystallinity, Fourier-transform infrared spectroscopy (FTIR) for functional groups and chemical bonds, Ultraviolet-Visible diffuse reflectance spectroscopy (UV-Vis DRS) to assess optical absorption and estimate the band gap, photoluminescence (PL) spectroscopy to analyze charge-carrier recombination, and field-emission scanning electron microscopy (FESEM) along with dispersive X-ray spectroscopy (EDX) for elemental composition. TEM and FESEM images confirmed the needle-shaped morphology and size of the nanostructures. This morphology contributed to faster degradation under natural sunlight. Their high photocatalytic efficiency arises from the anisotropic nanoneedle shape, which provides a large active surface area and promotes rapid charge transport, along with advantageous optical properties such as strong sunlight absorption and reduced electron–hole recombination. Overall, these features enable faster reaction kinetics, making $BaZrO_3$ nanoneedles a highly effective and durable photocatalyst for degrading both cationic and anionic pollutants. The photocatalytic performance was tested on two organic dyes: the cationic dye Rhodamine B (RhB) and the anionic dye Indigo Carmine (IC). The nanoneedles achieved 99.5% degradation of RhB in 50 min and 98% of IC in 60 min, demonstrating excellent photocatalytic activity. These results confirm that $BaZrO_3$ nanoneedles are efficient photocatalysts for rapidly breaking down both cationic and anionic dye pollutants under sunlight.

Key words: Ultrasound cavitation technique; Nanoneedles; Optical properties; Photocatalyst; Rhodamine B (Rh B); Indigo carmine (IC)

Citation: Chavan H, Sudapalli A M., Badani P M. Ultrasound-Fabricated $BaZrO_3$ Nanoneedles for Degradation of Hazardous Organic Dyes. *Environmental Chemistry and Safety*, 2026, 2, 9600058. https://doi.org/10.26599/ECS.2025.9600058

1. Introduction

Perovskite oxides with the general formula ABO_3 have long attracted attention due to their diverse functional properties[1], including ferroelectricity[2], ionicconductivity[3], superconductivity[4], magnetism[5], and catalytic activity[6]. Recent studies increasingly highlight that the size [6-8], form effects [9-10], and nanostructured materials particles have been the focus of scientific and technological research on several applications [11]. Furthermore, tailoring the exposed crystal planes—even within the same crystal system—can significantly enhance the functional properties of metal oxide nanomaterials[12-14]. $BaZrO_3$ is a chemically robust perovskite, resistant to CO_2 poisoning and acidic corrosion, with excellent dielectric properties and high thermal stability. Despite these attributes, its use in photocatalysis has remained limited, mainly due to two persistent challenges: its wide bandgap (3.8–4.0 eV), which limits visible-light absorption, and the difficulty of synthesizing high-surface-area $BaZrO_3$ without high-temperature calcination. Conventional methods such as coprecipitation [15], hydrothermal[16-20], solvothermal[21-23], and sol–gel approaches[24-26] synthesis usually demand extended calcination steps at elevated temperatures, which not only consume significant energy but also lead to particle coarsening, irregular morphologies, and reduced surface area. To address these limitations, researchers have doped $BaZrO_3$ with cations (e.g., Bi, Mg, W, Cd) or incorporated co-catalysts to lower the band gap and enhance the photocatalytic response. While such modifications enhance activity, they also have drawbacks, such as dopant leaching, limited long-term stability, increased cost, and synthetic complexity that limit scalability. Furthermore, most reported $BaZrO_3$ photocatalysts have been tested only under UV illumination, whereas practical wastewater treatment requires robust activity under natural solar light.

Another underexplored dimension is morphology-directed photocatalysis. Previous studies have focused mainly on spherical or irregular $BaZrO_3$ particles, with limited attention given to anisotropic architectures. Morphologies such as nanoneedles can offer significant advantages, including extended surface areas for pollutant adsorption, one-dimensional pathways for charge transport that minimize recombination losses, and preferential facet exposure that enhances the generation of reactive oxygen species (ROS). However, a limited report has demonstrated ultrasound-assisted anisotropic growth of $BaZrO_3$. Ultrasound cavitation produces localized hot spots, high shear forces, and transient microjets that facili-

Correspondence to: Badani P M, pmbadani@chem.mu.ac.in
Received: October 30, 2025; Revised: December 8, 2025; Accepted: December 14, 2025

tate rapid nucleation and anisotropic growth without requiring surfactants, templates, or prolonged autoclaving. Importantly, ultrasound synthesis is calcination-free, energy-efficient, and environmentally benign, making it particularly attractive for sustainable nanomaterial fabrication.

In this context, the present work addresses two critical gaps: the lack of a green, one-step method for producing anisotropic $BaZrO_3$ nanostructures and the absence of studies demonstrating their visible-light photocatalytic activity under natural sunlight. We reportthe ultrasound-driven synthesis of $BaZrO_3$ nanoneedles that exhibit directional growth along the c-axis and a narrowed bandgap, bothof which are conducive to visible-light photocatalysis. The nanoneedles rapidly degrade both cationic (Rhodamine B) and anionic (Indigo Carmine) dyes under solar irradiation, achieving nearly complete removal within 1 hour. Radical scavenging experiments confirm that hydroxyl radicals and superoxide anions dominate the degradation mechanism, highlighting the role of anisotropy in facilitating efficient charge separation and ROS generation. Beyond morphology control, this work establishes ultrasound-driven anisotropy as a scalable, sustainable strategy to activate $BaZrO_3$ for solar photocatalysis. The twin novelties lie in the eco-friendly synthesis of nanoneedles without calcination or dopants and in the demonstration of fast dye degradation under real sunlight, positioning this study as an essential advance toward practical wastewater remediation using perovskite photocatalysts [27].

2. Experimental work

2.1. Chemicals and reagents

$BaCl_2.2H_2O$ (barium chloride dihydrate), $ZrOCl_2.8H_2O$ (zirconyl chloride octahydrate), sodium hydroxide (NaOH), Rhodamine B (RhB), and Indigo carmine (IC) dyes were purchased from Sigma Aldrich, Mumbai (India). All chemicals were of AR grade and used without purification. Distilled water was used throughout the experimentation.

2.2. Synthesis of $BaZrO_3$ nanoneedles

In deionized water, barium chloride dihydrate ($BaCl_2{\cdot}2H_2O$) and zirconyl chloride octahydrate ($ZrOCl_2{\cdot}8H_2O$) were dissolved in stoichiometric ratios (Ba:Zr = 1:1) while keeping the total cation content at 1 mol/dm^3. At room temperature, the resultant solution was magnetically agitated for 20 min. The pH was then gradually raised to 14 by applying ultrasonic irradiation and adding a 20 mol/dm^3 NaOH solution dropwise to the mixture. The resulting white precipitate was separated by centrifugation, thoroughly cleaned with deionized water, and allowed to dry overnight at 80°C following a 30 min ultrasonic treatment. In **Figure 1**, the entire $BaZrO_3$ nanoneedles production process is schematically presented.

2.3. Characterization

The structure of $BaZrO_3$ was ascertained at a scanning rate of 5° min^{-1} using an X-ray diffractometer (CuKα λ = 1.5418 Å, diffraction angle (2θ) - 10 to 90°, Shimadzu, Maxima 7000 S, Tokyo, Japan). The Debye Scherer equation was used to determine the mean particle size. The typical JCPDS sheet and the acquired data were contrasted. Functional groups in $BaZrO_3$ were identified from Fourier transform infrared (FTIR) spectra recorded on a Perkin-Elmer Frontier spectrometer (United Kingdom) over the range 400–4000 cm^{-1}. An ultraviolet-visible spectrophotometer (Shimadzu UV-2450) was used to record UV-Visible absorption spectra. The morphology of nanoparticles was examined using a FESEM (Carl Zeiss SMT AG, Germany). Size measurements were made using a transmission electron microscope (TEM, JEM-2100) device [27].

2.4. Photocatalytic study

The photocatalytic ability of $BaZrO_3$ was evaluated using the organic dyes RhB and IC as model pollutants.10 ppm (10 mg dye/L) of the dye solution was used. Using sunlight, the dye degradation process was investigated. $BaZrO_3$ (5 mg) was added to 50 mL of the dye solution (1.0×10^{-5} M). UV-Visible spectroscopy was used to analyze a small volume of the sample solution after a predetermined amount of time. The adsorption–desorption equilibrium was established by stirring the reaction mixture in the dark for 60 min, followed by exposure to sunlight for photocatalytic degradation. This formula calculated the efficiency of dye degradation.

$$Degradation(\%) = \left(1 - \frac{C}{C_0}\right) X100. \quad (1)$$

Where C_o is the dye's concentration in water before irradiation, and C is its concentration in water following a predetermined amount of irradiation. The rate constant of the reaction is determined using the Langmuir-Hinshelwood model.

$$ln\frac{C_0}{C} = k_{app}t \quad (2)$$

C_o is the initial dye concentration, and C is the final dye concentration following light exposure. k_{app} is a pseudo-first-order kinetic rate constant at time t. To ascertain whether the $BaZrO_3$ could be reused, the experiment was conducted four times in a row [28].

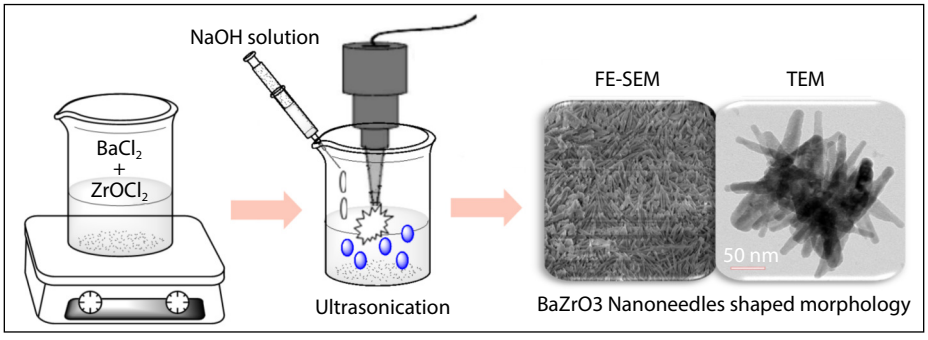

Fig. 1. Schematic representation for the synthesis of BaZrO3 nanoneedles

3. Results and discussion

3.1. Structural and optical studies

Figure 2(a) shows the diffraction peaks of the synthesized $BaZrO_3$ nanoneedles, which were indexed using JCPDS Card No. 06-0399, corresponding to the cubic perovskite structure (space group: $Pm\bar{3}m$). The major peaks observed at $2\theta \approx 22.1°$, 31.4°, 38.6°, 45.2°, and 55.6° match well with the (100), (110), (111), (200), and (211) planes reported in the JCPDS standard. The absence of secondary peaks confirms the phase purity of the synthesized material. These results are consistent with previous reports on crystalline $BaZrO_3$ nanoparticles. Indicating that the ultrasound cavitation route yields phase-pure products without post-calcination. Since $BaZrO_3$ nanoneedles exhibit only the cubic phase peak, they are likely pure. Sonication was used to create $BaZrO_3$ nanoneedles without the requirement for further heating or calcination. The crystallite size was calculated using Scherrer's formula and found to be approximately 30-32 nm. This nanoscale domain size is particularly significant, as it correlates with the anisotropic growth observed in FESEM/TEM and contributes to bandgap narrowing compared to bulk $BaZrO_3$. The absence of peak broadening beyond expected values suggests well-ordered crystallinity despite the low-temperature, rapid synthesis process—highlighting the effectiveness of ultrasound in directing controlled nucleation and growth. Fourier transform infrared (FTIR) spectra further corroborate the formation of $BaZrO_3$, as shown in **Figure 2 (b)**. The strong absorption band at ~505 cm^{-1} corresponds to Zr–O vibrations in the perovskite lattice, while the feature at 1457 cm^{-1} is attributed to Ba–O bonding. A broad band near 3475 cm^{-1} indicates surface hydroxyl groups, likely arising from adsorbed moisture. These hydroxyl groups are beneficial, as they provide anchoring sites for dye adsorption and can act as precursors for the generation of hydroxyl radicals (·OH) under illumination, thereby linking structural features to photocatalytic activity. Notably, the absence of carbonate-related peaks confirms that CO_2 contamination was avoided—a common problem in Ba-based perovskites synthesized by hydrothermal or sol–gel methods.

To evaluate the optical properties, UV–Vis (DRS) and the Tauc plot were used to estimate the bandgap as shown in **Figure 2(c–d)**. Bulk $BaZrO_3$ typically exhibits a bandgap in the range of ~4.0 to 5.0 eV [29], consistent with its classification as a wide-bandgap insulator. However, the nanoneedles displayed an optical bandgap of 3.26 eV, indicating a redshift into the near-visible region. This reduction can be attributed to nanoscale effects and anisotropic charge confinement, which enhance light harvesting across the solar spectrum. The observed shift in the absorption peak can be attributed to electrostatic interactions arising from the negatively charged surface of the $BaZrO_3$ nanoneedles, as confirmed by the zeta potential value of −41.3 mV. The narrowing of the bandgap is crucial, as it enables activation under natural sunlight, unlike bulk $BaZrO_3$ or doped systems that rely on artificial UV sources. This visible-light response directly correlates with the high photocatalytic efficiency observed. Visible-light-driven photocatalysts require the visible region of $BaZrO_3$ (λ_{max}= 326 nm). The equation relates the bandgap E_g to the wavelength λ: $E_g = 1240/\lambda$. The calculated bandgap of the sample is E_g = 3.80 eV. Therefore, in **Figure 2(d)**, the bandgap determined from the Tauc plot was 3.26 eV, which is less than the 3.80 eV bandgap of bulk $BaZrO_3$. Therefore, it confirms that the ultrasound-assisted synthesis did not significantly alter the intrinsic optical characteristics of the $BaZrO_3$ lattice. At the nanoscale, quantum confinement effects lower the bandgap. This finding implies that $BaZrO_3$ can serve as an effectivevisible-light photocatalyst. Because of its broad bandgap, light absorption, forma-

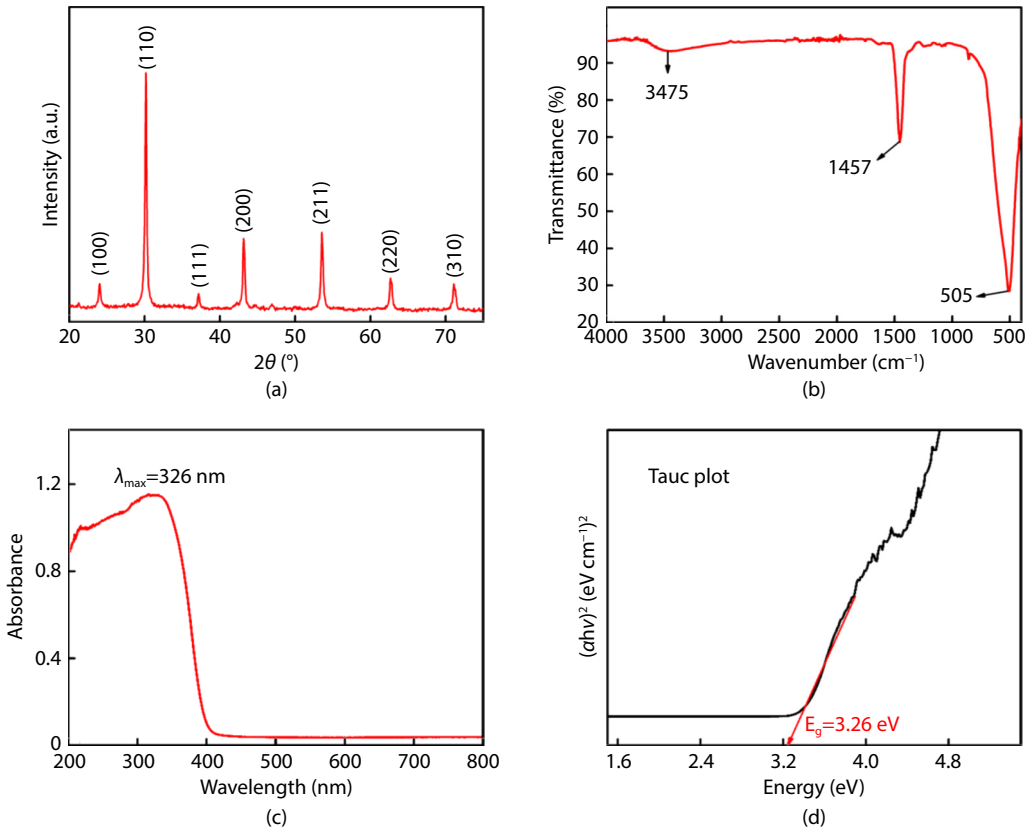

Fig. 2. (a) XRD, (b) FT-IR, (c)UV-Vis (DRS) of $BaZrO_3$ Nanoneedles, and (d)Tauc's plot.

tion of reactive charge carriers, chemical stability, surface reactivity, potential applications, and affordability, $BaZrO_3$ is a promising photocatalyst [30].

Figure 3 shows the Photoluminescence (PL) spectra to investigate defects in $BaZrO_3$, which analyzes the recombination efficiency between photogenerated holes (h^+) and electrons (e^-). The emission spectrum of $BaZrO_3$ (λ_{em}) is 356 nm, 462 nm, and 663 nm, as shown in Figure 3; there is a significant reduction in PL intensity over 350–670 nm, resulting in lower charge recombination rates and better charge-carrier separation, thereby increasing photocatalytic efficiency. Efficient charge separation could increase the lifetime of charge carriers by enhancing interfacial charge transfer to adsorbed substrates, thereby improving photocatalytic activity[31]. All these suggest enhanced photocatalytic activity of $BaZrO_3$ nanoneedles.

3.2. Morphological studies

Morphological analysis by FESEM revealed the formation of uniform nanoneedles, typically several hundred nanometers in length, with diameters in the tens of nanometers **Figure 4 (a–b)**. Such anisotropy is rarely reported for $BaZrO_3$ synthesized without templates or surfactants, underscoring the unique effect of ultrasound cavitation. The needle-like morphology provides a high surface-to-volume ratio, thereby increasing the number of adsorption sites for pollutant molecules. **Figure 4 (c)** shows that Energy-dispersive X-ray spectroscopy (EDX) confirmed the elemental composition, detecting only Ba, Zr, and O, further supporting the phase purity of the synthesized material. Furthermore, as demonstrated in **Figure 5 (a-**

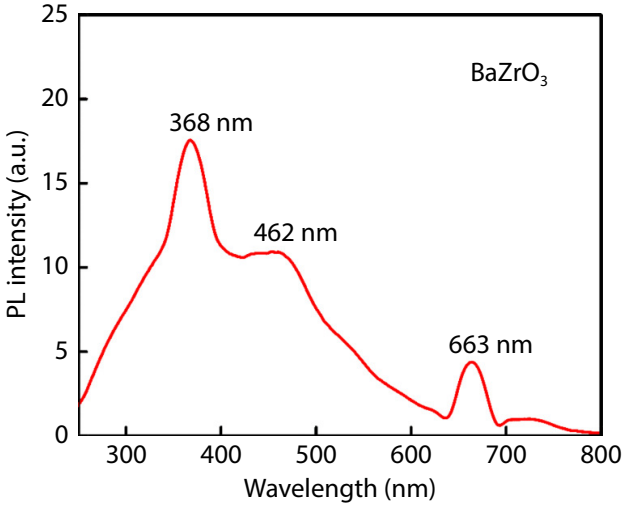

Fig. 3. spectra of $BaZrO_3$ Nanoneedles

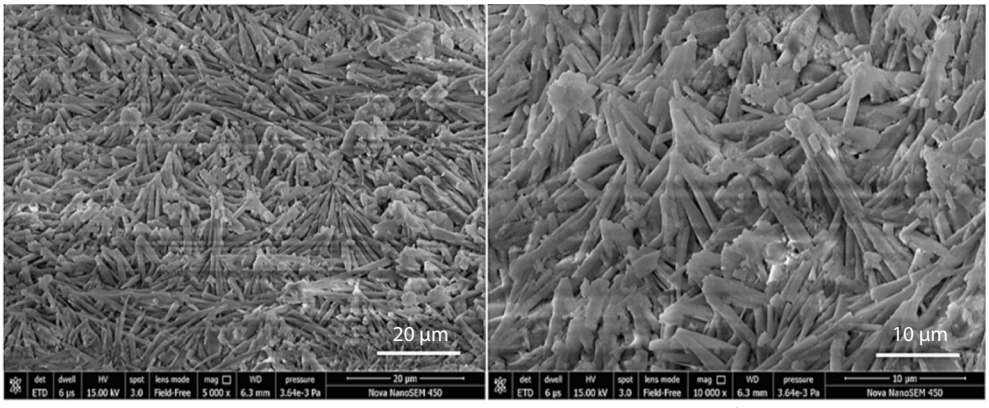

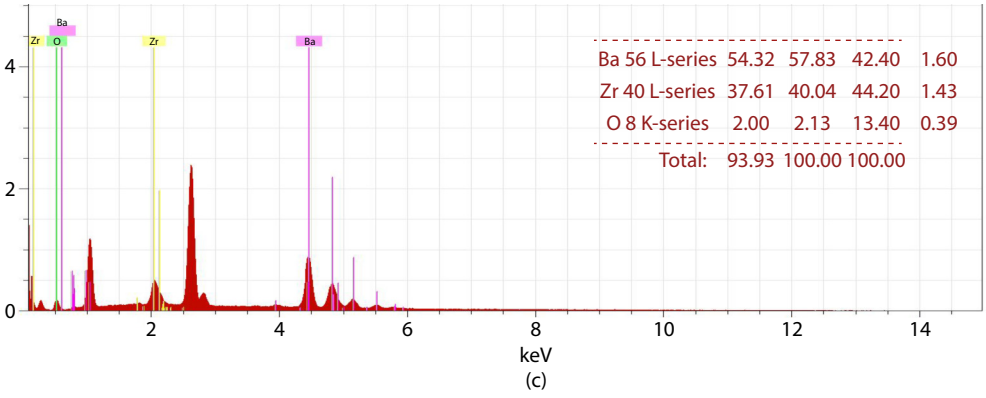

Fig. 4. (a-b) FESEM under low magnification (20 µm and 10 µm) showing nanoneedles morphology, (c) EDX spectrum of $BaZrO_3$ nanoneedles

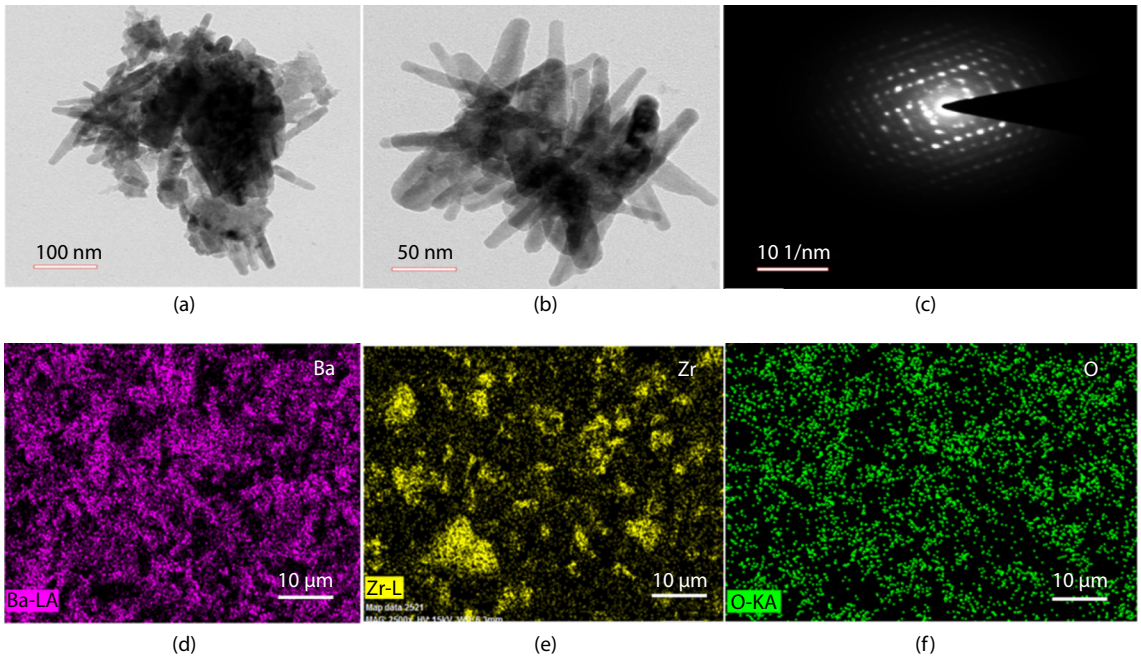

Fig. 5. (a-b) HRTEM under high magnification (100 nm and 50 nm), (c) SAED pattern, and (d-f) Elemental mapping of $BaZrO_3$ nanoneedles

b), HRTEM images confirm the formation of a nanoneedle morphology, showing elongated structures originating from particle nucleation; this observation is further supported by FESEM analysis. Therefore, it confirmed the one-dimensional anisotropic growth, showing well-resolved lattice fringes consistent with the cubic $BaZrO_3$ structure. The selected region of the electron diffraction pattern (SAED) aligns with the obtained XRD result. The SAED pattern **in Figure 5(c)** shows well-defined diffraction rings corresponding to the (100), (110), (111), and (200) planes of cubic $BaZrO_3$, indicating the polycrystalline nature of the nanoneedles. The measured interplanar spacings (d-spacings) closely match those obtained from XRD analysis, further validating the phase purity. **Figure 5 (d-f)** shows the corresponding elemental mapping for Ba, Zr, and O. The elemental mapping result indicates that all of the elements are evenly distributed throughout the sample [32]. These results establish a strong correlation between synthesis conditions, structure, and photocatalytic performance. The ultrasound-induced anisotropy not only directs the growth of $BaZrO_3$ into nanoneedles but also produces a narrowed bandgap, surface hydroxylation, and high crystallinity—all of which synergistically enhance visible-light absorption, charge-carrier separation, and dye adsorption. These structural and optical features directly rationalize the rapid photocatalysis observed in subsequent studies.

3.3. DLS and Zeta Potential Studies

Figure 6 shows the Dynamic Light Scattering (DLS) analysis of $BaZrO_3$, which involves dispersing the particles in water and detecting the fluctuations in scattered light induced by their Brownian motion. This examination can reveal the particle size distribution. The DLS analysis of the size distribution of $BaZrO_3$ nanoneedles corroborated the XRD and TEM results. To understand the characteristics and behaviour of $BaZrO_3$ nanoneedles-for catalyst applications.

Zeta potential measurements have been conducted to determine the surface charge of synthesized $BaZrO_3$ nanoneedles. Generally, zeta potential is used to analyze biomolecular stability and nanoparticle interactions. **Figure7** shows the surface charges on $BaZrO_3$ nanoneedles, with zeta potentials ranging from –41 to –41.3 mV. The zeta potential indicates that the samples are stable.

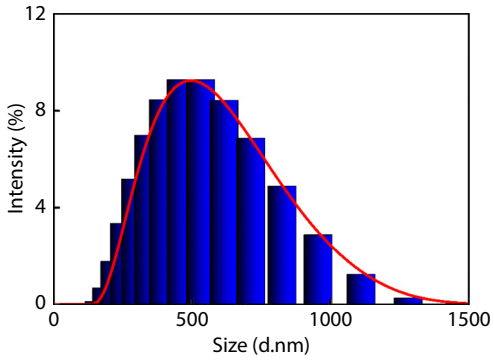

Fig. 6. DLS of $BaZrO_3$ Nanoneedles

3.4. Photocatalytic activity

Indigo Carmine (IC), an anionic dye, and Rhodamine B (RhB), a cationic dye, were selected as model organic pollutants. Using $BaZrO_3$ nanoneedles exposed to sunlight, the effects of industrial pollutants from textiles and dyes were examined. Photocatalytic experiments were performed under natural sunlight between 11:30 AM and 2:00 PM in May, on clear, cloudless days with high solar irradiance.

Figures 8(a) and 8(c) show the de-dying procedure; both dyes were observed in the blank studies without a photocatalyst. RhBand IC dye solutions in water are exceptionally stable since sunlight only slightly alters the dyes' color. The degradation of dyes requires an appropriate photocatalyst.

To distinguish adsorption effects from photocatalytic degradation, the dye–catalyst suspensions were stirred in the dark for 60 min to reach adsorption–desorption equilibrium. The adsorption data indicated that $BaZrO_3$ nanoneedles removed only 23% of RhB and 12% of IC in the dark, demonstrating minimal adsorption of the dye molecules on the catalyst surface. After illumination, the degradation significantly increased to

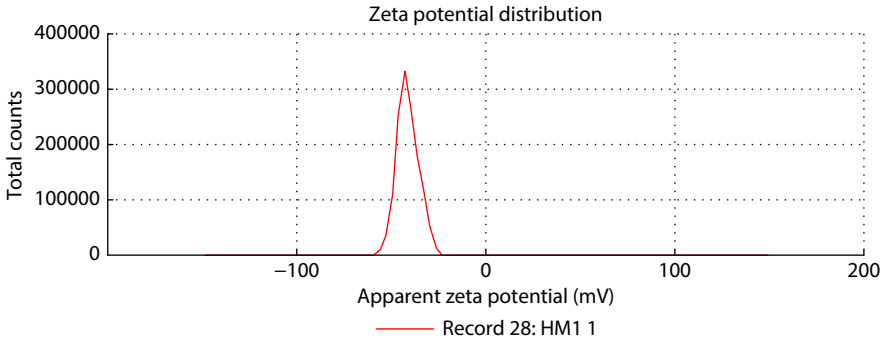

Fig. 7. Zeta potential of $BaZrO_3$ Nanoneedles

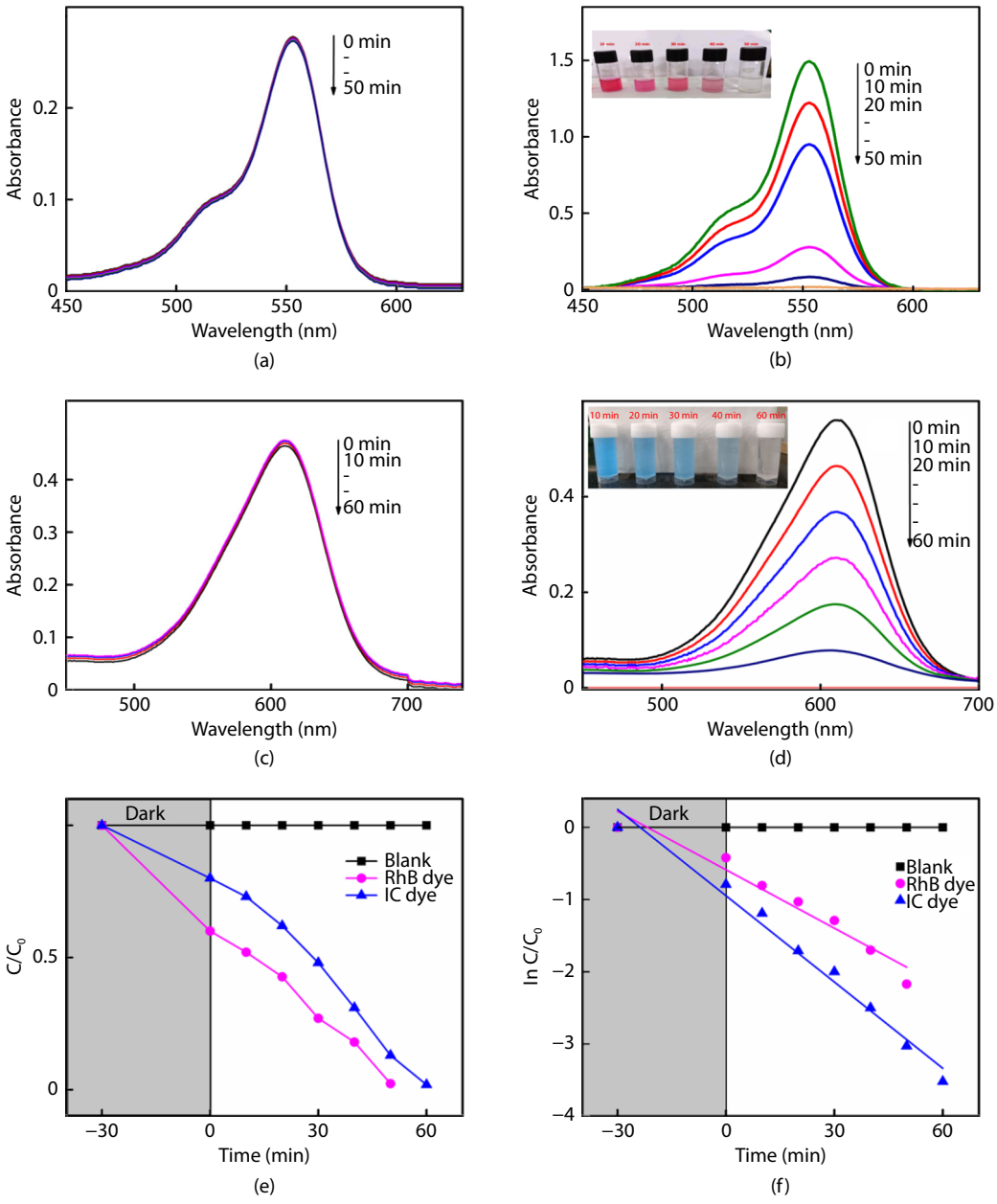

Fig. 8. (a) Blank dye RhB (b) Absorbance spectra of RhB (c) Blank IC dye (d) Absorbance spectra IC (e–f) Kinetic study of RhB and IC by using $BaZrO_3$ nanoneedles as photocatalyst

99.5% for RhB and 98% for IC, confirming that the observed dye removal predominantly arises from photocatalytic activity rather than dark adsorption. These results align with the typical behavior of wide-band-gap perovskite oxides, where photocatalysis is the dominant removal mechanism.

To investigate the photocatalytic activity, $BaZrO_3$ nanoneedles were then added to the dye solution. To achieve saturation adsorption equilibrium, the material was agitated in the

dark for 60 min. The absorption spectra were then recorded every 10 min after the sample was exposed to direct sunlight. At 550 nm, RhB exhibited an absorption peak. After 50 min of photodegradation, the $BaZrO_3$ nanoneedles' absorbance maxima disappeared, as seen in **Figure 8(b)**. The IC dye's peak absorption spectrum, displayed in **Figure 8(d)**, peaked at 610 nm and then decreased significantly after 60 min. Under typical conditions, sunlight degrades RhB and IC dyes similarly. Furthermore, the shift in absorption peak intensity supports the presence of a negative charge on the surfaces of the $BaZrO_3$ nanoneedles, as indicated by the zeta potential measurements. Because RhB dye is cationic, electrostatic interactions and forces play a significant role in its rapid degradation [33]. RhB degrades in under 50 min, whereas IC takes 10 min longer, according to **equation (1)**. **Figure 8 (e) and (f)** employ the Langmuir-Hinshelwood formulation **equation (2)** to display pseudo-first-order kinetics, denoted by a straight line. The $BaZrO_3$ nanoneedles' apparent rate constant (k_{1app}) for RhB dyes is 0.0020 min^{-1} (R^2 = 0.981), while for IC dyes it is 0.0018 min^{-1} (R^2 = 0.986), according to pseudo-first-order kinetics. Based on these findings, $BaZrO_3$ nanoneedles are reasonably active at photodegrading both dyes.

3.5. Reusability and stability studies

A photocatalyst's utility in commercial and industrial contexts is high, particularly in terms of stability and reusability. Therefore, despite reducing costs, the durability and reusability of the photocatalyst should be evaluated. After degrading RhB and IC in sunlight, the potential for reusing $BaZrO_3$ nanoneedles was assessed. RhB and IC can be broken down by recycling the produced $BaZrO_3$ nanoneedles four times, as shown in **Figure 9 (a)**. Additionally, to remove the degraded dye nanoparticles from the catalyst's surface, the catalyst was rinsed with an ethanol-deionized water solution after the experiment. After drying, it was subjected to the same testing procedures again. Following four cycles, RhB's photocatalytic activity was 79%, whereas IC's was 76%. After four cycles, the $BaZrO_3$ nanoneedles continue to perform more efficiently and exhibit outstanding photocatalytic activity[34].

Additionally, after four cycles, agglomeration of BaZrO3 nanoneedles was observed. The Fourier transform infrared spectra of the pure dye and its solution following degradation by a $BaZrO_3$ nanoneedle photocatalyst are shown in **Figure 9(c–f)**. The results indicate that the $BaZrO_3$ photocatalyst was effective, as evidenced by the significantly shifted peak. A pure and

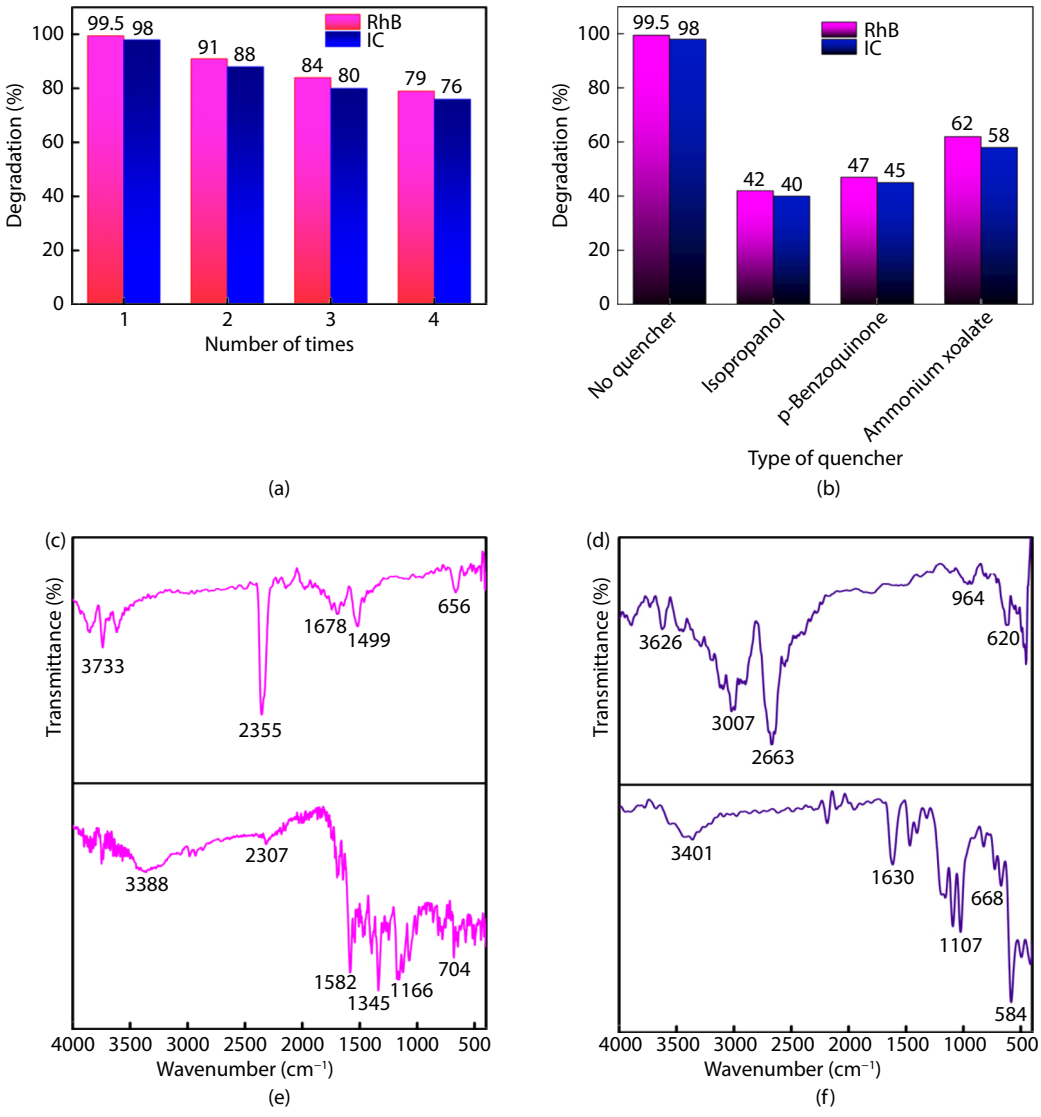

Fig. 9. (a) Degradation behavior of RhB and IC at variable cycles (b) Photodegradation caused by the effect of quenchers RhB and IC dye using $BaZrO_3$, FT-IR spectrum of (c) Degraded RhB, (d) Degraded IC, (e) RhB dye, and (f) IC dye

post-degradation dye with a functional group ofRhB and IC dye group is shown in **Table 1,** along with the FTIR peak location descriptions.

XRD analysis was performed on $BaZrO_3$ nanoneedles after the fourth cycle. $BaZrO_3$ nanoneedles. Changes in peak position, alterations in intensity, or the emergence of new peaks may be visible in XRD patterns during the reuse of photocatalysts. Crystallite size fluctuations and phase transitions are examples of changes in crystal structure, as seen in **Figure 10(a)**. As illustrated in **Figure 10(b)**, FT-IR spectra can reveal changes in peak positions or intensities, as well as the emergence or disappearance of peaks associated with functional groups during reuse. After the fourth cycle, the morphologies of the RhB and IC nanoneedles were observed by FESEM, as shown in Figures 10**(c)** and 10**(d)**.

3.6. Mechanistic insights of dye degradation

Many reactive radicals, including holes (h^+), hydroxyl radicals ($^{\bullet}OH$), and superoxide anion radicals ($O_2^{\bullet-}$), are in charge of the photocatalytic destruction of a dye. To understand the mechanisms of photocatalytic reactions, it is crucial to investigate the reactive radicals that drive the degradation process [35]. To examine the effect of radical scavengers on the degradation of RhB and IC dyes under visible-light exposure, trapping experiments were performed. In this work, photogenerated $O_2^{\bullet-}$, $^{\bullet}OH$, and h^+ were quenched using benzoquinone (BQ), isopropanol (IPA), and ammonium oxalate (AO). Without a scavenging intermediate, the highest photocatalytic degradation of RhB dye (99.5%) and IC dye (98%) was accomplished, as seen in **Figure 9(b)**. IPA was added, and the $^{\bullet}OH$ radical significantly reduced the degradation of both dyes, suggesting that it is essential for photocatalytic degradation. The photodegradation decreased from 98.5% to 47% in RhB and from 98% to 45% in IC when BQ was introduced, indicating that $O_2^{\bullet-}$ is a secondary oxidative species. In the meantime, AO showed a slight decrease, suggesting that h^+ was the most active species. Therefore, it was determined that the influencing order was $^{\bullet}OH > O_2^{\bullet-} > h^+$. The scavenging study results suggest that the improved photocatalytic mechanism of $BaZrO_3$ nanoneedles, which may be described as follows:

$$BaZrO_3 + hv \rightarrow BaZrO_3\ (e^-_{cb}) + BaZrO_3\ (h^+_{vb})$$

$$BaZrO_3\ (e^-_{cb}) + O_2 \rightarrow BaZrO_3 + O_2^{\cdot-}$$

$$BaZrO_3\ (h^+_{vb}) + OH^- \rightarrow OH^{\bullet}$$

$$O_2^{\cdot-} + H_2O \rightarrow OH^- + HO_2^{\cdot}$$

$$HO_2^{\cdot} + H_2O \rightarrow OH^{\bullet} + H_2O_2$$

Table 1. Functional group analysis of RhB and IC dyes (before and after degradation)

Characteristic peak (cm^{-1})		Functional group	Characteristic peak (cm^{-1})		Functional group
RhB dye	Degraded RhB		IC dye	Degraded IC	
3388	3733	O–H stretching	3401	3626	O–H stretching
2307	2355	C=C stretching	-	3007	C=C stretching
1582	1678	C=C stretching	-	2663	C–H stretching
1345	1499	C–O stretching	1630	-	C–O stretching
1166	-	C–O stretching	1107	964	C–O-C stretching
704	-	C–H stretching	668	620	N–H stretching
-	656	N–H stretching	584	-	CH-HStretching

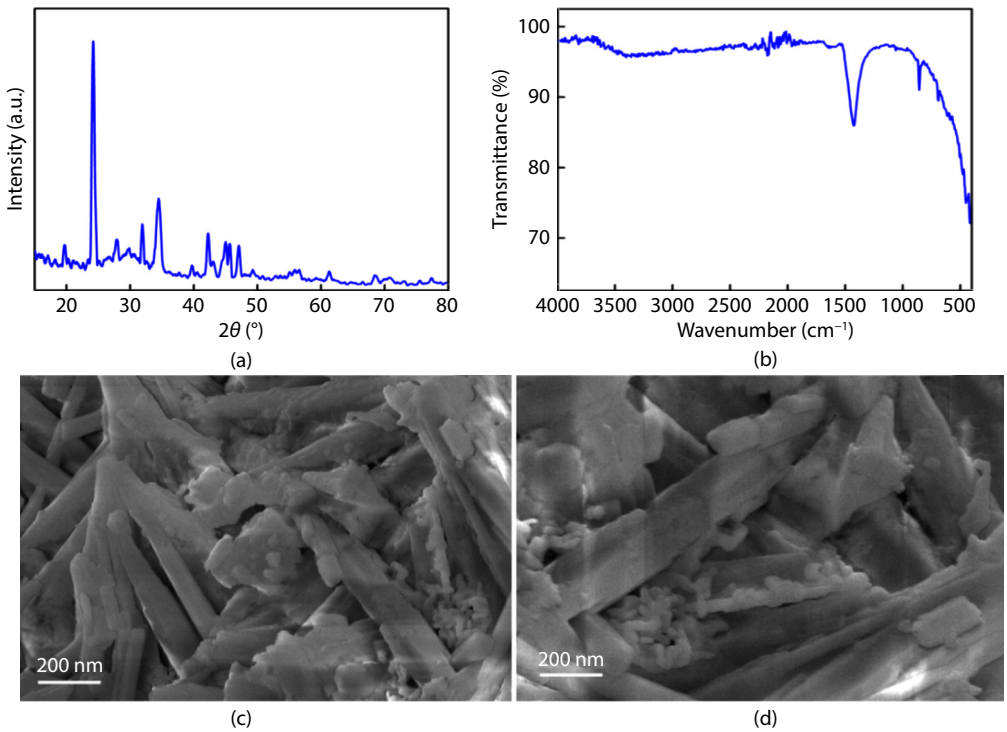

Fig. 10. (a–b) XRD and FTIR of recovered photocatalyst (4th cycle), (c–d) FESEM of (4th cycle)

$H_2O_2 \rightarrow 2OH^{\cdot}$

Dye (RhB / IC) + $OH^{\cdot} \rightarrow CO_{2\uparrow} + H_2O$ + degraded products

The photocatalytic reaction mechanism was examined to identify the reactive species responsible for dye degradation. When exposed to sunlight, the photocatalyst is excited from the valence band to the conduction band, generatingelectrons in the conduction band and holes in the valence band. Consequently, photogenerated holes and electrons migrate toward the nanoparticles' surface. In experiments, these excitons can form a superoxide radical anion by directly reacting with the dye, resulting in the production of oxidized products and dissolved oxygen. Similarly, upon radiation exposure, these photogenerated holes may migrate toward the surface and directly react with the dye, producingdegraded intermediates.

As shown in **Figure 11**, the surface hydroxyl groups are engaged with both electrons and holes at the VB and CB, respectively. The highly oxidative nature of holes and $OH^{\cdot}$ radicals causes dyes to partially or entirely deteriorate. The production of hydroxyl radicals ($OH^{\cdot}$), a key component of photocatalytic activity, is enhanced. When sunlight strikes $BaZrO_3$ nanoneedles at 3.26 eV, electrons in the valence band are excited to the newly created Zr^{4+} and Ba^{2+} states. Superoxide radical anions ($O_2^{\cdot-}$) were produced by induced electrons interacting with dissolved oxygen molecules. These anions were then protonated to make hydroperoxyl radicals ($HO_2^{\cdot}$), which in turn were protonated to form hydroxyl radicals ($OH^{\cdot}$). But on surface adsorbed water, the hydroxyl radicals produced by the holes will react with RhB and IC. The dyes are oxidized by the formation of the hydroxyl radical, producing harmless byproducts such as CO_2 and H_2O, as well as degradation products[36].

Table 2 provides a comparative summary of different $BaZrO_3$-based photocatalysts reported in the literature, along with their degradation performance toward various organic dyes. The catalysts include pristine $BaZrO_3$, doped variants (W-doped and Mg-doped $BaZrO_3$), and $BaZrO_3$:Bi, each tested against pollutants such as tetracycline (TC), phenol, methylene blue (MB), and Congo red (CR). The reduction time needed for dye degradation ranges from 60 min to 6 hours, with degradation efficiencies from 80% to 100%, depending on the catalyst and target dye. Notably, pristine $BaZrO_3$ achieves complete phenol degradation in 60 min, while doped versions show improved kinetics and efficiency for other dyes. In comparison, the current study demonstrates superior photocatalytic activity with $BaZrO_3$ nanoneedles, achieving rapid degradation of Rhodamine B (RhB) and Indigo Carmine (IC) within 50 and 60 min, respectively, with efficiencies of 99.5% and 98%, respectively. The nanoneedle morphology of $BaZrO_3$ provides a larger active surface area and improved charge-transfer pathways, enabling faster and more effective dye degradation.

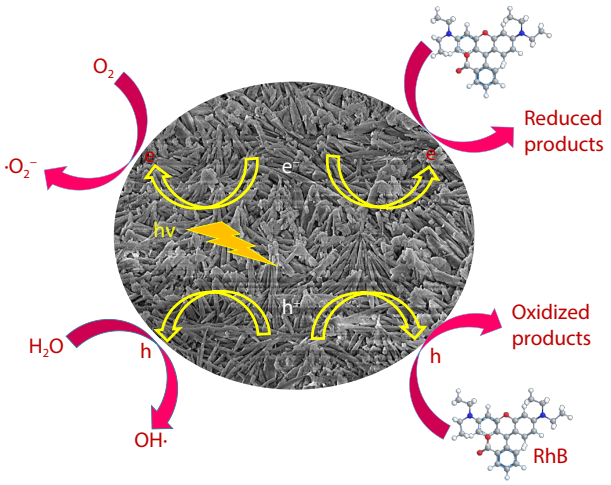

Fig. 11. Degradation mechanism of dye using $BaZrO_3$ nanoneedles

4. Conclusion

The ultrasonic cavitation method was successfully used to produce $BaZrO_3$ nanoneedles. The ultrasound is essential to the development of nanoparticles. It is beneficial for structuring surface-active molecules and is made to bind them onto various crystal planes of nucleating centers. TEM and XRD analyses revealed a crystallite size of ~30–32 nm, indicating that the uniform ultrasonic treatment facilitated the formation of needle-like structures, as confirmed by TEM and FESEM images, with no impurity detected. Photocatalytic degradation of the cationic dye RhB and the anionic dye IC under solar radiation was studied. $BaZrO_3$ nanoneedles degraded RhB dye within 50 min, achieving99.5% catalytic efficiency. Concurrently, IC dye was broken down in 60 min with 98% efficiency. Four successive cycles yielded 79% efficiency for RhB and 76% for IC, indicating strong reusability. The morphology-dependent photocatalytic activity of $BaZrO_3$ was observed, and numerous attempts were made to enhance its photoactivity by altering its morphology. This study established an effective technique for creating $BaZrO_3$ nanoneedles. With minimal energy and cost-effectiveness, it can effectively inhibit harmful ionic dyes and clean wastewater in large-scale processing.

Conflict of Interest

Authors declare no conflict of interest.

Acknowledgement

The authors are grateful for the characterization facilities provided by the Micro-analytical Laboratory, Department of Chem-

Table 2. Comparative study of photocatalytic activity of $BaZrO_3$ towards different dyes

Catalyst	Dyes	Reduction time	% Degradation	References
W doped $BaZrO_3$	TC	180 min	94.9%	[37]
$BaZrO_3$	Phenol	60 min	100%	[38]
$BaZrO_3$:Bi	MB	6 hours	87.5%	[39]
Mg doped $BaZrO_3$	MB	180 min	80%	[40]
$BaZrO_3$	CR	250 min	84.1%	[41]
$BaZrO_3$ Nanoneedles	**RhB** **IC**	**50 min** **60 min**	**99.5%** **98%**	**Present study**

istry, University of Mumbai.

References

[1] Xu, J. T.; Yan, X. Y.; Reng, X. J.; Dong, R. Y.; Chu, Y. X.; Zheng, Y. K.; Wang, K. Q.; Wu, Y.; He, Y. M. Ultrasound-driven S-scheme g-C3N5/$Bi_4Ti_3O_{12}$ heterojunctions for enhanced piezocatalytic degradation of organic dyes. *J. Environ. Chem. Eng.*, 2025, 13: 118386.

[2] Song, W. L.; Lee, B. I.; Zhong, L. W.; Samuels, W. D. Hydrothermal synthesis and structural characterization of $BaTiO_3$ nanocrystals. *J. Cryst. Growth*, 2000, 219: 269–276.

[3] Iwahara, H. Oxide-ionic and protonic conductors based on perovskite-type oxides and their possible applications. *Solid State Ion.*, 1992, 52: 99–104.

[4] Ohkubo, M.; Hioki, T. $YBa_2Cu_3O_x$ superconducting thin-film formation studied by Rutherford backscattering spectroscopy for the multilayer deposition method. *Jpn. J. Appl. Phys.*, 1988, 27: L613.

[5] Wollan, E. O.; Koehler, W. C. Neutron diffraction study of the magnetic properties of the series of perovskite-type compounds [(1-x)La, xCa] MnO_3. *Phys. Rev.*, 1955, 100: 545–563.

[6] Kanie, K.; Seino, Y.; Matsubara, M.; Muramatsu, A. Size-controlled hydrothermal synthesis of monodispersed $BaZrO_3$ sphere particles by seeding. *Adv. Powder Technol.*, 2017, 28: 55–60.

[7] Kovalenko, M. V.; Kaufmann, E.; Pachinger, D.; Roither, J.; Huber, M.; Stangl, J.; Hesser, G.; Schäffler, F.; Heiss, W. Colloidal HgTe nanocrystals with widely tunable narrow band gap energies: from telecommunications to molecular vibrations. *J. Am. Chem. Soc.*, 2006, 128(11): 3516–3517.

[8] Wada, S.; Yasuno, H.; Hoshina, T.; Kakemoto, H.; Kameshima, Y.; Tsurumi, T. Size dependence of THz region dielectric properties for barium titanate fine particles. *J. Electroceram.*, 2008, 21: 198–201.

[9] Jiang, B.; Peng, J. L.; Bursill, L. A.; Zhong, W. L. Size effects on ferroelectricity of ultrafine particles of $PbTiO_3$. *J. Appl. Phys.*, 2000, 87: 3462–3467.

[10] Hong, G. Y.; Jeon, B. S.; Yoo, Y. K.; Yoo, J. S. Photoluminescence characteristics of spherical Y_2O_3: Eu phosphors by aerosol pyrolysis. *J. Electrochem. Soc.*, 2001, 148: H161.

[11] Kimijima, T.; Sasaki, T.; Nakaya, M.; Kanie, K.; Muramatsu, A. Photocatalytic activity of Ni-loaded TiO_2 nanoparticles precisely controlled in size and shape. *Chem. Lett.*, 2010, 39: 1080–1081.

[12] Ogi, T.; Nandiyanto, A. B. D.; Okuyama, K. Nanostructuring strategies in functional fine-particle synthesis towards resource and energy saving applications. *Adv. Powder Technol.*, 2014, 25: 3–17.

[13] Kimijima, T.; Kanie, K.; Nakaya, M.; Muramatsu, A. Solvothermal synthesis of $SrTiO_3$ nanoparticles precisely controlled in surface crystal planes and their photocatalytic activity. *Appl. Catal. B Environ.*, 2014, 144: 462–467.

[14] Yang, H. G.; Sun, C. H.; Qiao, S. Z.; Zou, J.; Liu, G.; Smith, S. C.; Cheng, H. M.; Lu, G. Q. Anatase TiO_2 single crystals with a large percentage of reactive facets. *Nature*, 2008, 453: 638–641.

[15] Hai, B.; Shukla, A. K.; Duncan, H.; Chen, G. Y. The effect of particle surface facets on the kinetic properties of $LiMn_{1.5}Ni_{0.5}O_4$ cathode materials. *J. Mater. Chem. A*, 2013, 1: 759–769.

[16] Boschini, F.; Rulmont, A.; Cloots, R.; Vertruyen, B. Rapid synthesis of submicron crystalline barium zirconate $BaZrO_3$ by precipitation in aqueous basic solution below 100°C. *J. Eur. Ceram. Soc.*, 2009, 29: 1457–1462.

[17] Lu, Z. G.; Tang, Y. G.; Chen, L. M.; Li, Y. D. Shape-controlled synthesis and characterization of $BaZrO_3$ microcrystals. *J. Cryst. Growth*, 2004, 266: 539–544.

[18] Dias, A.; Ciminelli, V. S. T. Electroceramic materials of tailored phase and morphology by hydrothermal technology. *Chem. Mater.*, 2003, 15(6): 1344–1352.

[19] Dong, Z. H.; Ye, T. N.; Zhao, Y. N.; Yu, J. G.; Wang, F. Q.; Zhang, L. L.; Wang, X. B.; Guo, S. K. Perovskite $BaZrO_3$ hollow micro- and nanospheres: Controllable fabrication, photoluminescence and adsorption of reactive dyes. *J. Mater. Chem.*, 2011, 21: 5978–5984.

[20] Kanie, K.; Seino, Y.; Matsubara, M.; Nakaya, M.; Muramatsu, A. Hydrothermal synthesis of $BaZrO_3$ fine particles controlled in size and shape and fluorescence behavior by europium doping. *New J. Chem.*, 2014, 38: 3548–3555.

[21] Özeren, Y.; Mensur-Alkoy, E.; Alkoy, S. Sodium niobate particles with controlled morphology synthesized by hydrothermal method and their use as templates in KNN fibers. *Adv. Powder Technol.*, 2014, 25: 1825–1833.

[22] Niederberger, M.; Pinna, N.; Polleux, J.; Antonietti, M. A general soft-chemistry route to perovskites and related materials: Synthesis of $BaTiO_3$, $BaZrO_3$, and $LiNbO_3$ nanoparticles. *Angew. Chem. Int. Ed.*, 2004, 43: 2270–2273.

[23] K. Nakashima, T. Goto, S. Iwatsuki, M. Kera, I. Fujii, S. Wada, Preparation of BaZrO3 nanoparticles using a solvothermal reaction, in: IOP Conf. Ser. Mater. Sci. Eng., IOP Publishing, 2011: p. 92049.

[24] Nakashima, K.; Fujii, I.; Wada, S. Preparation of $BaZrO_3$ cubes by composite-hydroxide-mediated approach at low temperature. *J. Ceram. Soc. Japan*, 2011, 119: 532–534.

[25] Liu, R. Z.; Zhao, Y. J.; Zhou, H. P. A general approach to monodisperse perovskite microspheres. *Adv. Powder Technol.*, 2014, 25: 780–786.

[26] Prastomo, N.; Zakaria, N. H. B.; Kawamura, G.; Muto, H.; Sakai, M.; Matsuda, A. High surface area $BaZrO_3$ photocatalyst prepared by base-hot-water treatment. *J. Eur. Ceram. Soc.*, 2011, 31: 2699–2705.

[27] Zhou, Y. J.; Chu, Y. X.; Lin, Y.; Gong, C. Y.; Xu, L. W.; Wang, K. Q.; He, Y. M.; Wu, Y. Harvesting vibration energy for efficiently piezocatalytic degradation of organic dyes by $Bi_{11}VO_{19}$ nanosheets. *J. Clean. Prod.*, 2025, 521: 146189.

[28] Veith, M.; Mathur, S.; Lecerf, N.; Huch, V.; Decker, T.; Beck, H. P.; Eiser, W.; Haberkorn, R. Sol-gel synthesis of nano-scaled $BaTiO_3$, $BaZrO_3$ and $BaTi_{0.5}Zr_{0.5}O_3$ oxides via single-source alkoxide precursors and semi-alkoxide routes. *J. Sol Gel Sci. Technol.*, 2000, 17: 145–158.

[29] Yuan, Y. P.; Zhang, X. L.; Liu, L. F.; Jiang, X. J.; Lv, J.; Li, Z. S.; Zou, Z. G. Synthesis and photocatalytic characterization of a new photocatalyst $BaZrO_3$. *Int. J. Hydrog. Energy*, 2008, 33: 5941–5946.

[30] Sudapalli, A. M.; Shimpi, N. G. Ag@rGO coral reef morphology exhibits excellent optical properties and photocatalytic activity against methyl orange under sunlight. *Diam. Relat. Mater.*, 2023, 139: 110356.

[31] Sudapalli, A.; Shimpi, N. Investigation of the photocatalytic activity of electrospun and surface-modified PAN/α-FeOOH nanofibers for the degradation of hazardous azo dyes. *Langmuir*, 2023, 39(44): 15517–15534.

[32] Rizwan, M.; Aleena, S.; Shakil, M.; Mahmood, T.; Ahmad Zafar, A.; Hussain, T.; Farooq, M. H. A computational insight of electronic and optical properties of Cd-doped $BaZrO_3$. *Chin. J. Phys.*, 2020, 66: 318–326.

[33] Sudapalli, A. M.; Shimpi, N. G. 3D ZnO sunstar rose nanoflowers morphology with surfactant-assisted reflux exhibit excellent optical properties and photocatalytic activity against hazardous organic dyes. *Opt. Mater.*, 2023, 136: 113391.

[34] Sudapalli, A. M.; Shimpi, N. G. Hierarchical self-assembly of 0D/2D β-Bi_2O_3 crossandra flower morphology exhibits excellent photocatalytic activity against bromophenol dyes. *Opt. Mater.*, 2022, 132: 112849.

[35] Sudapalli, A. M.; Shimpi, N. G. Tetragonal SnO_2 nanoparticles: An efficient photocatalyst for the degradation of hazardous ionic dyes. *ChemistrySelect*, 2023, 8: e202203310.

[36] Sudapalli, A. M.; Shimpi, N. G. Hydrothermal synthesis of α-FeOOH (1D) nanorods and their transition to α-Fe_2O_3 (0D): An efficient photocatalyst in neutralizing hazardous organic dyes. *New J. Chem.*, 2023, 47: 14323–14334.

[37] Gulen, B.; Demircivi, P.; Simsek, E. B. UV-a light irradiated photocatalytic performance of hydrothermally obtained W doped $BaZrO_3$ catalyst against the degradation of levofloxacin and tetracycline antibiotic. *J. Photochem. Photobiol. A Chem.*, 2021, 404: 112869.

[38] Miodyńska, M.; Bajorowicz, B.; Mazierski, P.; Lisowski, W.; Klimczuk, T.; Winiarski, M. J.; Zaleska-Medynska, A.; Nadolna, J. Preparation and photocatalytic properties of $BaZrO_3$ and $SrZrO_3$ modified with Cu_2O/Bi_2O_3 quantum dots. *Solid State Sci.*, 2017, 74: 13–23.

[39] Borja-Urby, R.; Díaz-Torres, L. A.; Salas, P.; Moctezuma, E.; Vega, M.; Ángeles-Chávez, C. Structural study, photoluminescence, and photocatalytic activity of semiconducting $BaZrO_3$: Bi nanocrystals. *Mater. Sci. Eng. B*, 2011, 176: 1382–1387.

[40] Ma, X. L.; Zhang, J. C.; Li, H. H.; Duan, B. C.; Guo, L. N.; Que, M. D.; Wang, Y. H. Violet blue long-lasting phosphorescence properties of Mg-doped $BaZrO_3$ and its ability to assist photocatalysis. *J. Alloys Compd.*, 2013, 580: 564–569.

[41] Kayathiri, C.; Balu, A. R.; Suganya, M.; Vinitha, G.; Delci, Z.; Balamurugan, S.; Karthika, M.; Anitha, S.; Prabavathi, A. $BaZrO_3$ perovskite–A UV light mediated Congo red dye deactivator catalyst with good optical switching and antimicrobial abilities green synthesized using *Moringa oleifera* leaf extract. *Mater. Sci. Eng. B*, 2022, 278: 115636.